

Controlling secondary flow in Taylor–Couette turbulence through spanwise-varying roughness

Dennis Bakhuis¹, Rodrigo Ezeta¹, Pieter Berghout¹,
Pim A. Bullee^{1,2}, Dominic Tai¹, Daniel Chung³, Roberto Verzicco^{4,1},
Detlef Lohse^{1,5}, Sander G. Huisman¹, and Chao Sun^{6,1}†

¹Physics of Fluids Group, Max Planck UT Center for Complex Fluid Dynamics,
MESA+ Institute and J.M. Burgers Centre for Fluid Dynamics,
University of Twente, P.O. Box 217, 7500 AE Enschede, The Netherlands

²Soft matter, Fluidics and Interfaces, MESA+ Institute for Nanotechnology,
University of Twente, P.O. Box 217, 7500 AE Enschede, The Netherlands

³Department of Mechanical Engineering, University of Melbourne, Victoria 3010, Australia

⁴Dipartimento di Ingegneria Industriale, University of Rome Tor Vergata,
Via del Politecnico 1, Rome 00133, Italy

⁵Max Planck Institute for Dynamics and Self-Organization, Am Faßberg 17, Göttingen,
Germany

⁶Center for Combustion Energy, Key Laboratory for Thermal Science and Power Engineering
of Ministry of Education, Department of Energy and Power Engineering, Tsinghua University,
Beijing, China

(Received xx; revised xx; accepted xx)

Highly turbulent Taylor–Couette flow with spanwise-varying roughness is investigated experimentally and numerically (direct numerical simulations (DNS) with an immersed boundary method (IBM)) to determine the effects of the spacing and axial width s of the spanwise varying roughness on the total drag and on the flow structures. We apply sandgrain roughness, in the form of alternating rough and smooth bands to the inner cylinder. Numerically, the Taylor number is $\mathcal{O}(10^9)$ and the roughness width is varied between $0.47 \leq \tilde{s} = s/d \leq 1.23$, where d is the gap width. Experimentally, we explore $Ta = \mathcal{O}(10^{12})$ and $0.61 \leq \tilde{s} \leq 3.74$. For both approaches the radius ratio is fixed at $\eta = r_i/r_o = 0.716$, with r_i and r_o the radius of the inner and outer cylinder respectively. We present how the global transport properties and the local flow structures depend on the boundary conditions set by the roughness spacing \tilde{s} . Both numerically and experimentally, we find a maximum in the angular momentum transport as function of \tilde{s} . This can be attributed to the re-arrangement of the large-scale structures triggered by the presence of the rough stripes, leading to correspondingly large-scale turbulent vortices.

Key words: Turbulent flow: Turbulence control, Boundary Layers: Boundary layer structure

1. Introduction

In nearly all industrial applications and geophysical flows, turbulence is partly or

† Email address for correspondence: chaosun@tsinghua.edu.cn

completely wall-bounded. In general, boundaries are not smooth but their surface is rather irregular and rough. Accordingly, such flows are extensively studied, although mainly under the approximation that the roughness is *homogeneous* (Jiménez 2004). Homogeneously rough surfaces have a characteristic length scale k that is much smaller than the largest wall normal length scale δ . The effects of the roughness in these flows is believed to be confined to the immediate vicinity of the wall (i.e. the roughness sublayer), whereas in the outer, inertial layer, the flow only experiences the effective shear stress of the surface (Townsend’s outer layer similarity, Townsend (1976)). As such, the focus of many studies is to find functional relationships between the parameters describing the roughness geometry and the skin friction coefficient C_f (Flack & Schultz 2010). In practice, however, flows are bounded by rough boundaries that, not only vary on the scale of k , but also on a much larger scale s , being $s = \mathcal{O}(\delta)$. Whereas these variations can occur either laterally (spanwise) or longitudinally (streamwise), we focus here only on the former. Such examples are found in shipping (i.e. the formation of stripes of biofouling on ship hulls (Schultz 2007)) and geophysical flows (e.g. the atmospheric flows over spanwise-varying terrain (Ren & Wu 2011)).

Hitherto, the research is focused on the effects of spanwise-varying rough surfaces on canonical systems of wall-bounded turbulence research, i.e. pipe- (Koeltzsch *et al.* 2002), boundary layer- (Anderson *et al.* 2015), and channel-flow (Chung *et al.* 2018). The hallmark of flows over these surfaces is the presence of spanwise wall-normal secondary flows of size $\mathcal{O}(\delta)$, with mean streamwise vorticity. Examples of studies where this has been observed are the works of Koeltzsch *et al.* (2002) on the effects of convergent and divergent grooves (reminiscent of shark skin) and the work by Wang & Cheng (2006) on spanwise-varying riverbeds. We note that earlier research dates back to the works of Hinze (1967, 1973) in the field of surface stress variations in duct flows.

Following up on the work of Koeltzsch *et al.* (2002), Nugroho *et al.* (2013) set out to perform a parametric study of the converging-diverging riblets surface in a zero pressure gradient boundary layer (BL). They find a thickening of the BL height above the converging regions, and vice versa above the diverging regions. Furthermore, the energy spectra show an increased energy content of the larger scales. Barros & Christensen (2014) performed stereo particle image velocimetry (PIV) in the spanwise wall-normal plane for the flow over a turbine blade replica and found spanwise variations of the order δ in the mean velocity field. Within the same configuration, Mejia-Alvarez & Christensen (2013) identified regions of low momentum pathways (LMPs) and high momentum pathways (HMPs) in the instantaneous fields. Here, LMPs coincide with regions of enhanced turbulent kinetic energy (TKE) and Reynolds shear stress (RSS), and rather remarkably, these regions do seem to occur at recessed roughness heights. Willingham *et al.* (2014) found very similar behaviour of the secondary flows for a much more regular surface geometry. Vanderwel & Ganapathisubramani (2015) found that only when $s/\delta \gtrsim 0.5$, where s is the spacing between streamwise aligned Lego[®] blocks, secondary flow formation is observed. However, for $s/\delta \lesssim 0.5$ the secondary flows are confined to the roughness sublayer. Interestingly, contrary to the findings of Mejia-Alvarez & Christensen (2013), they find LMPs on top of their elevated blocks, and HMPs in between the roughness strips. Yang & Anderson (2017), however, found $s/H \gtrsim 0.2$, with H the channel half height, as the threshold for heterogeneous behaviour of the streamwise aligned pyramid elements. By carefully assessing the terms in the transport equation TKE, Anderson *et al.* (2015) found that spanwise variations of roughness lead to a local imbalance of production and dissipation of TKE, as already proposed by Hinze (1967). Since the secondary flows are driven by a spatial gradient of the RSS, they find that the mean secondary flows are Prandtl’s secondary flow of the second kind (Bradshaw

1987). Medjnoun *et al.* (2018) observed a breakdown of outer layer similarity in the local profiles of the mean flow, turbulent intensity, and the energy spectra, evidently induced by the presence of the secondary vortices. Finally, Chung *et al.* (2018) studied the influence of the spacing of idealized (i.e. no geometric induced disturbances to the flow) regions of low shear stress and high shear stress. They find that for $s/\delta \lesssim 0.39$ the notion of outer layer similarity is retained. Interestingly, for $s/\delta \gtrsim 6.28$, they find a sign reversal of the isovels (stream velocity contour lines), with respect to the orientation of the secondary flows, that remain upwelling over low shear stress regions.

The aforementioned studies were all carried out in systems that lack two features which are intrinsic to many applications, namely the curvature in the streamwise direction (as in turbine blades), and the presence of strong secondary motions (as in the atmospheric boundary layer).

A canonical system in which these two properties can be observed simultaneously is the Taylor–Couette (TC) flow. TC flow is the flow between two coaxially, independently rotating cylinders. Its geometry is characterized by the inner cylinder radius r_i , outer cylinder radius r_o , and their axial length L , described by two dimensionless parameters; the radius ratio $\eta = r_i/r_o$ and the aspect ratio $\Gamma = L/d$, where $d = r_o - r_i$ is the gap width between the cylinders. Since TC is a closed system, one can directly relate global and local quantities through exact mathematical relations (Eckhardt *et al.* 2007). The driving strength in TC flow is expressed in dimensionless form by the Taylor number:

$$\text{Ta} = \frac{1}{4} \sigma d^2 \frac{(r_i + r_o)^2 (\omega_i - \omega_o)^2}{\nu^2}, \quad (1.1)$$

where $\omega_{i,o}$ are the inner and outer angular velocity of the cylinders, respectively, ν is the kinematic viscosity of the fluid, and $\sigma = ((1 + \eta) / (2\sqrt{\eta}))^4$ is the so-called geometric Prandtl number, in analogy to the Prandtl number in Rayleigh–Bénard convection (Eckhardt *et al.* 2007). Alternatively, when the outer cylinder is at rest ($\omega_o = 0$), the driving strength can also be expressed with a Reynolds number based on the inner scales $\text{Re}_i = r_i \omega_i d / \nu$. This Reynolds number and Ta ($\omega_o = 0$), are related by $\text{Re}_i = (8\eta^2 / (1 + \eta)^3) \sqrt{\text{Ta}}$. In TC flow, the angular velocity flux J^ω is radially conserved. Here, $J^\omega = r^3 (\langle u_r \omega \rangle_{A,t} - \nu \frac{\partial}{\partial r} \langle \omega \rangle_{A,t})$, where the brackets $\langle \cdot \rangle_{A,t}$ denote averaging over a cylindrical surface and time. The angular momentum flux for the case of laminar flow is $J_{lam}^\omega = 2\nu r_i^2 r_o^2 (\omega_i - \omega_o) / (r_o^2 - r_i^2)$. In this way the response of the flow is quantified by the dimensionless Nusselt number (Nu_ω), which is also directly related to the torque \mathcal{T} that is required to drive the cylinders at constant speed, i.e.

$$\text{Nu}_\omega = \frac{J^\omega}{J_{lam}^\omega} = \frac{\mathcal{T}}{2\pi L \rho J_{lam}^\omega}. \quad (1.2)$$

Here, ρ is the density of the working fluid. Alternatively, the torque of the system can be non-dimensionalized to form the friction coefficient $C_f = \mathcal{T} / (\rho L \nu^2 \text{Re}_i^2)$, which is directly related to the Nusselt number:

$$\text{Nu}_\omega = C_f \omega_i (r_o - r_i)^2 (r_o^2 - r_i^2) / (4\pi \nu r_o^2). \quad (1.3)$$

The inner friction velocity $u_{\tau,i}$ is also related to the torque by $u_{\tau,i} = \sqrt{\mathcal{T} / (2\pi r_i^2 \rho L)}$, which is used to scale quantities in the inner layer. Lastly, a frictional Reynolds number based on the inner scales can be defined as $\text{Re}_\tau = u_{\tau,i} d / (2\nu)$.

Secondary flows are featured in TC flow, in the form of large scale vortices with a mean streamwise vorticity component, the so-called Turbulent Taylor Vortices (TTV). These structures are reminiscent of laminar Taylor vortices, which transition through a series of instabilities into turbulence once the flow becomes unstable (Taylor 1923).

As noted by Chouippe *et al.* (2014), the axial wavelength λ/d of the TTVs, *i.e.* the distance between two rolls, is primarily a function of η and Re . When Re is large enough ($\mathcal{O}(10^6)$), the rolls are observed to persist in the system (Huisman *et al.* 2014). Here, multiple states for $\eta = 0.716$ can be observed in a certain regime of counter-rotating cylinders, namely $a \in [0.17, 0.51]$, where $a = -\omega_o/\omega_i$ is their rotation ratio. These multiple states are characterized by a change in the number of rolls present in the system and, as a consequence, in their averaged axial wavelength ($\lambda/d = 1.46$ or $\lambda/d = 1.96$). These states, with the transition between them being strongly hysteretic, even at $\text{Re} = \mathcal{O}(10^6)$ (Huisman *et al.* 2014; van der Veen *et al.* 2016), result in different torques for the same rotation rates, which reflects the importance of the large scale structures (TTV) in transporting angular momentum. At pure inner cylinder rotation however ($a = 0$), no multiple states are found and the rolls are observed to be less coherent and stable. Finally, we note that the effect of the curvature of the cylinders is quantified by the radius ratio η , and it has a tremendous impact on the flow organization as was reported by Ostilla-Mónico *et al.* (2014*a,b*). For a detailed review on turbulent Taylor-Couette flow we refer the reader to Grossmann *et al.* (2016).

Roughness in a TC geometry has been studied in various ways: Cadot *et al.* (1997); van den Berg *et al.* (2003) used obstacle roughness, in the form of axial riblets, to study the scaling of the angular momentum transport with the driving strength. Zhu *et al.* (2016) investigated the influence of grooves for large Ta ($\mathcal{O}(10^{10})$), and find that at the tips of the grooves, plumes are preferentially ejected. In a more recent work, Zhu *et al.* (2018) find that by using a similar configuration of rough walls as van den Berg *et al.* (2003), the scaling $\text{Nu}_\omega \propto \text{Ta}^{1/2}$ predicted by the so-called asymptotic ultimate regime can be achieved. They attribute this to a dominance of the pressure drag over the viscous drag on the cylinders. Very recently, Berghout *et al.* (2018) studied the influence of sandgrain roughness in TC flow, and found similarity of the roughness function with the same type of roughness in pipe flow Nikuradse (1933). None of the TC papers described above reported an influence of the roughness variations in the axial direction, *i.e.* the spanwise direction.

In this manuscript we will fill this gap and study the effects of spanwise-varying roughness in highly turbulent TC flow with Ta up to $\mathcal{O}(10^{12})$, for the case of pure inner cylinder rotation $a = 0$, where secondary flows are present in the form of TTVs. In particular, we focus on the effect of spanwise-varying roughness on the TTVs and thus, on the global and local response of the flow. We introduce the roughness through a series of stripes which extend along the entire circumference of the inner cylinder (IC). This gives rise to a spanwise (axial) arrangement of roughness which we characterize with the widths of the roughness stripe. We conduct both, experiments and direct numerical simulations (DNS) for various dimensionless stripe widths $\tilde{s} = s/d$, *i.e.* the width of the roughness stripe normalized with the gap width. The spacing between the roughness stripes is identical to the stripe width, thus a period consisting of one rough and smooth area has a width of $2\tilde{s}$.

The structure of the manuscript is as follows. In section 2 we introduce the experimental and numerical methods. In section 3.1 we show the local response of the flow due to the varying roughness arrangement. In section 3.2, we study its effect on the global quantities. In section 3.3 we link the global and local observations and explain the physical mechanism between the interaction of the rolls and the roughness. We finalize the manuscript in section 4 with some conclusions and an outlook to future work.

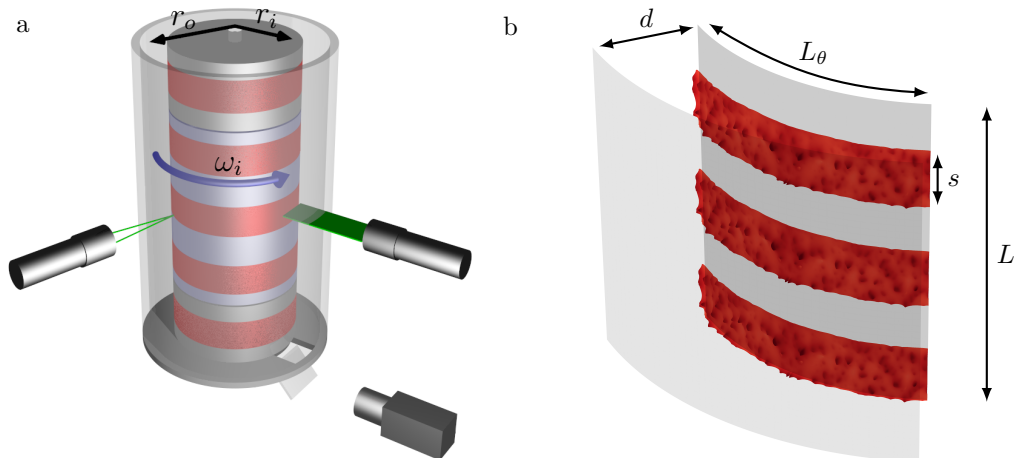


Figure 1: a) Schematic of the Twente Turbulent Taylor–Couette facility showing the sand paper roughness on the inner cylinder in red. PIV measurements in the r – θ plane become possible thanks to illumination from the side with a high-power pulsed laser, creating a horizontal sheet. The sheet is imaged through a window in the bottom. Using LDA the azimuthal velocity is measured along the axial direction. The torque is measured in the middle section of the IC, which has a length of $L_{mid} = 536$ mm. b) Numerical domain for the case of $\tilde{s} \equiv s/d = 0.47$. The sandpaper roughness is taken from a confocal scan of the material used in the experiment, see figure 2.

2. Methods

2.1 Experimental apparatus with spanwise roughness

The experiments have been performed in the Twente Turbulent Taylor–Couette (T³C) facility as shown in figure 1a (details of the experimental facility can be found in van Gils *et al.* (2011)). The inner cylinder has a radius $r_i = 200$ mm and the outer cylinder has a radius $r_o = 279.4$ mm, such that the gap size is $d = r_o - r_i = 79.4$ mm, and the radius ratio $\eta = 0.716$. The length of the cylinders is $L = 927$ mm, which leads to an aspect ratio $\Gamma = L/d = 11.7$. The outer cylinder (OC), is made of transparent acrylic which allows for optical access to the flow. The working fluid is demineralised water. We apply axially varying roughness to the inner cylinder (IC), which leads to patterns of uniformly rough and hydrodynamically smooth bands in the spanwise direction (see figure 1a). The rough stripes are made of P36 ceramic industrial grade sandpaper and are fixed to the IC using double-sided adhesive tape. In figure 2, we show the height scan of a roughness element using confocal microscopy. The scan revealed that the height (h_r) of the roughness is mostly within $\pm 2\sigma(h_r)$ of the mean, giving a characteristic length scale $k \equiv 4\sigma(h_r) = 695$ μm (see figure 2b). More statistics of the roughness is shown in table 1. We fix the surface coverage of the roughness at 56% such that $0.56A_i$ of the cylinder is rough, where $A_i = 2\pi r_i L$ is the area of the entire IC. The torque is only measured in the middle section of the IC, for which the roughness surface coverage is also 56% (see figure 1a).

2.1.1 Global measurements: Torque

We measured the torque \mathcal{T} needed to drive the inner cylinder at constant angular velocity (the outer cylinder is kept at rest). For this we used a hollow flange reaction torque transducer connecting the drive shaft and the inner cylinder. We continuously

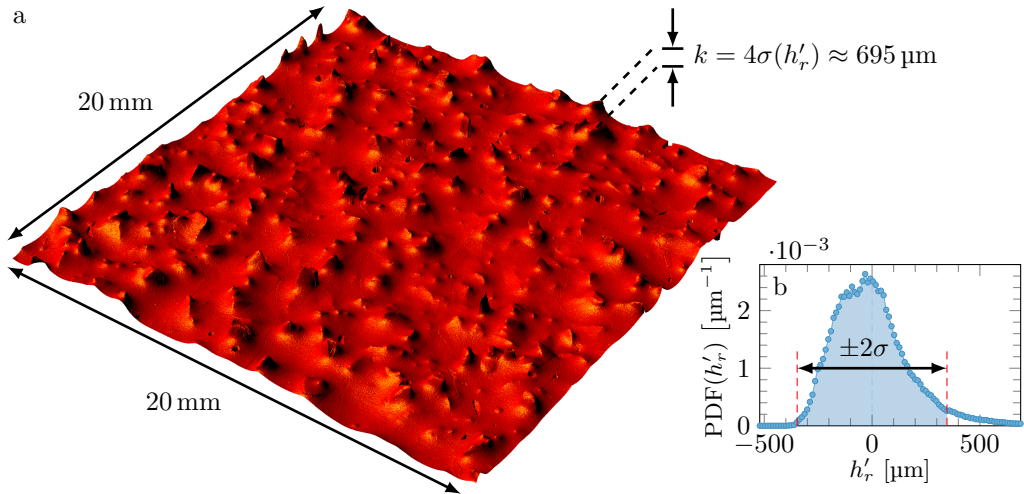


Figure 2: a) Height scan captured using confocal microscopy of a patch of sandpaper of $20 \text{ mm} \times 20 \text{ mm}$ with a resolution of $2.5 \mu\text{m}$. The typical size of the grains is given by $k \equiv 4\sigma(h'_r) = 695 \mu\text{m}$ where h'_r is the height and σ the standard deviation. The normalized typical grain size is then $k/d \approx 0.01$. b) Probability density function (PDF) of the measured height of the roughness stripe, with subtracted mean $h'_r = h_r - \langle h_r \rangle$.

Metric	Value
$\sigma(h_r) = \sqrt{\langle h_r'^2 \rangle}$	174 μm
$\langle h_r' \rangle$	134 μm
$\min(h_r')$	-527 μm
$\max(h_r')$	738 μm
$\text{median}(h_r')$	-19.6 μm
$\text{mode}(h_r')$	-27 μm
$\text{IQR} = Q3 - Q1 = \text{CDF}^{-1}(0.75) - \text{CDF}^{-1}(0.25)$	215 μm
$\langle h_r'^3 \rangle / \langle h_r'^2 \rangle^{3/2}$	0.928
$\langle h_r'^4 \rangle / \langle h_r'^2 \rangle^2$	4.361
wetted area / flat area	≈ 1.6
h_{smooth}	-1837 μm

Table 1: Various statistics of the roughness $h'_r = h_r - \langle h_r \rangle$ based on the data obtained from confocal microscopy, see also figure 2. h_{smooth} is the distance to the smooth cylinder surface, relative to $\langle h_r \rangle$. These values represent the actual roughness used in experiments; in DNS a scaled version of these values are used.

measured the torque while quasi-statically ramping the frequency of the inner cylinder, f_i , from 5 Hz to 18 Hz. This corresponds to $\text{Ta} \approx 4 \times 10^{11}$ and $\text{Ta} \approx 6 \times 10^{12}$ for the case of water as the working fluid. All the experiments were performed at $21 \pm 1 \text{ }^\circ\text{C}$ and all fluid flow properties are calculated at their actual temperature. Table 2 shows additional experimental parameters.

2.1.2 Local measurements: LDA and PIV

We performed an axial scan of the azimuthal velocity with laser Doppler anemometry (LDA). The scan was performed at the middle of the gap, $\tilde{r} = (r - r_i)/d = 0.5$, at a fixed $Ta = 9.5 \times 10^{11}$. The flow was seeded using $5\ \mu\text{m}$ -diameter polyamide particles with a density of $1030\ \text{kg m}^{-3}$ that act as tracers (van Gils *et al.* 2012). The laser beams went through the outer cylinder and were focused in the middle of the gap. We corrected for curvature effects by numerically ray tracing the LDA beams as was shown in Huisman *et al.* (2012). The axial extent of the LDA scans was $0 \leq z/L \leq 0.5$. Particle image velocimetry (PIV) measurements were performed at $Ta = 9.5 \times 10^{11}$ (same as LDA) in the radial-azimuthal plane. The scan was performed for various heights and for all \tilde{s} . For the PIV measurements the flow was seeded with different particles, namely, fluorescent polymer particles (Dantec FPP-RhB-10) with diameters of $1\text{--}20\ \mu\text{m}$ with a seeding density of ≈ 0.01 particles/pixel. These particles have an emission peak with a wavelength of $\approx 565\ \text{nm}$. We illuminated the particles with a Quantel Evergreen 145 532 nm, double pulsed laser. A cylindrical lens was used to create a light sheet of $\approx 1\ \text{mm}$ thickness. The images were captured with an Imager sCMOS ($2560 \times 2160\ \text{pixel}$) 16 bit camera with a Carl Zeiss 2.0/100 lens. The camera was operated in double frame mode with a frame rate f which was much smaller than the inverse interframe time $1/\Delta t$, i.e. $\Delta t \ll 1/f$. In order to enhance the particle contrast in the images, we added an Edmund High-Performance Longpass 550 nm filter to the camera lens. For every \tilde{s} , the axial extent of the experiments was different. This is done because—as will be shown later—the aspect ratio of the rolls change depending on \tilde{s} . For the smallest $\tilde{s} = 0.63$ however, the axial resolution was $\delta z/L \approx 0.011$ while for the largest value $\tilde{s} = 3.74$, $\delta z/L \approx 0.022$. Since we scan in the axial direction, the focus of the camera was changed accordingly. The fields were resolved with a commercial PIV software (Davis 8.0) based on a multi-step method. The initial window size was set to 64×64 pixels and it decreased to 32×32 pixels for the last iteration. The fields are calculated in Cartesian coordinates, which we transformed to polar coordinates. The final result were the fields in the form $\vec{u} = u_r(r, \theta, t)\hat{e}_r + u_\theta(r, \theta, t)\hat{e}_\theta$, where u_r and u_θ are the radial and azimuthal velocity component which depend on the radius r , the azimuthal (streamwise) direction θ , and time t .

2.2 Numerical methods

The Navier-Stokes (NS) equations were spatially discretized by using a central second-order finite-difference scheme and solved in cylindrical coordinates by a semi-implicit procedure (Verzicco & Orlandi 1996; van der Poel *et al.* 2015). The staggered grid is homogeneous in both the spanwise and streamwise directions (the axial and azimuthal directions, respectively). The wall-normal grid consists of a modified double cosine (Chebychev-type) mesh distribution. Below the maximum roughness height, we employed a cosine stretching such that the maximum grid spacing was always smaller than 0.5 times the viscous length scale $\delta_\nu = \nu/u_\tau$. In the bulk of the fluid, we employed a second stretching, such that the maximum radial grid spacing in the bulk is $\approx 1.7\delta_\nu$. The smallest radial mesh was $\approx 0.33\delta_\nu$, and is located at the position of the maximum roughness height, where we expect the highest shear stress. In table 2, we show a summary of the relevant run parameters. Time advancement was performed by using a fractional-step third-order Runge–Kutta scheme in combination with a Crank–Nicolson scheme for the implicit terms. The Courant–Friedrichs–Lewy (CFL) $(u\Delta t)/(\Delta x) < 0.8$ time-step constraint for the non-linear terms was enforced to ensure stability. We scale the roughness stripe such that the maximum roughness height, and thus the maximum

\tilde{s}	$N_\theta \times N_z \times N_r$	Ta	Γ	Re_τ	C_f	Nu_w	$\Delta(\omega)^+$	Δr_{\min}^+	Δr_{\max}^+	t_{av}/T
Simulations		$\times 10^9$								
Smooth	$758 \times 600 \times 840$	2.39	2.08	697	0.049	30.1	—	0.28	2.44	100
0.47	$1324 \times 1275 \times 1200$	1.33	2.52	686	0.084	38.9	6.36	0.33	1.76	43
0.61	$1324 \times 1121 \times 1200$	1.33	2.22	690	0.085	39.4	6.78	0.33	1.77	42
0.93	$1324 \times 1682 \times 1200$	1.45	3.32	692	0.079	38.1	6.21	0.33	1.77	42
1.23	$1324 \times 1121 \times 1200$	1.37	2.22	685	0.082	38.3	6.20	0.33	1.75	30
Rough	$1324 \times 1012 \times 1200$	1.19	2.00	689	0.095	41.5	8.11	0.33	1.76	43
Experiments		$\times 10^{12}$			$\times 10^3$					
Smooth		1.00	11.7	10.1	0.024	307				
0.61		1.00	11.7	13.0	0.041	509				
0.93		1.00	11.7	13.3	0.043	534				
1.23		1.00	11.7	13.0	0.041	508				
1.87		1.00	11.7	12.8	0.039	491				
3.74		1.00	11.7	13.1	0.041	517				
Rough		1.00	11.7	13.9	0.046	578				

Table 2: List of parameters involved in both the simulations and the experiments. $\tilde{s} = s/d$ is the normalized roughness width with smooth and rough indicating the fully smooth and fully rough case respectively. $N_\theta \times N_z \times N_r$ is the numerical resolution in the azimuthal, axial, and radial direction, respectively. $\Gamma = L/d$ the aspect ratio and $L_\theta = r_i \frac{1}{3} \pi$ is the constant azimuthal length of the domain. $\Delta(\omega)^+$ is the downward shift of the angular velocity profile ω^+ . Δr_{\min}^+ is the minimum spacing in the wall normal direction at the location of the maximum roughness height. Δr_{\max}^+ is the maximum spacing in the wall normal direction. $r_i^+ \Delta\theta = \Delta z^+ \approx 2.7$ ($r_o^+ \Delta\theta \approx 3.8$) is the grid spacing in the streamwise and spanwise directions. In the DNS, the roughness height $k^+ = 4\sigma(h_r)^+ = 130 \pm 1$ for all rough cases. t_{av}/T is the averaging time needed to collect statistics, normalized with the bulk flow time scale $T = d/(r_i(\omega_i - \omega_o))$.

blockage ratio, was $\max(h_r) = 0.1d$. Depending on \tilde{s} , we cut out a portion of roughness from the scanned surface. The roughness was then mirrored and concatenated to obtain a streamwise homogeneous spanwise periodic stripe. The streamwise and spanwise lengths of the computational domain are set to match the minimum computational domain size as studied in Ostilla-Mónico *et al.* (2014c). A moving average over 10×10 points is employed to smooth the scan from measurement noise. Finally, we set the resolution based on the demands ($\Delta z^+, r_i^+ \Delta\theta < 3$), which is small enough to recover the smallest geometrical features of the surface. The sandpaper roughness was implemented in the code by an immersed boundary method (IBM) (Fadlun *et al.* 2000). In the IBM, the boundary conditions were enforced by adding a body force \mathbf{f} to the Navier-Stokes equations. A regular, non-body fitting, mesh can thus be used, even though the rough boundary has a very complex geometry. We perform interpolation in the spatial direction preferential to the normal surface vector to transfer the boundary conditions to the momentum equations. The IBM has been validated previously (Fadlun *et al.* 2000; Iaccarino & Verzicco 2003; Stringano *et al.* 2006; Zhu *et al.* 2016, 2017, 2018).

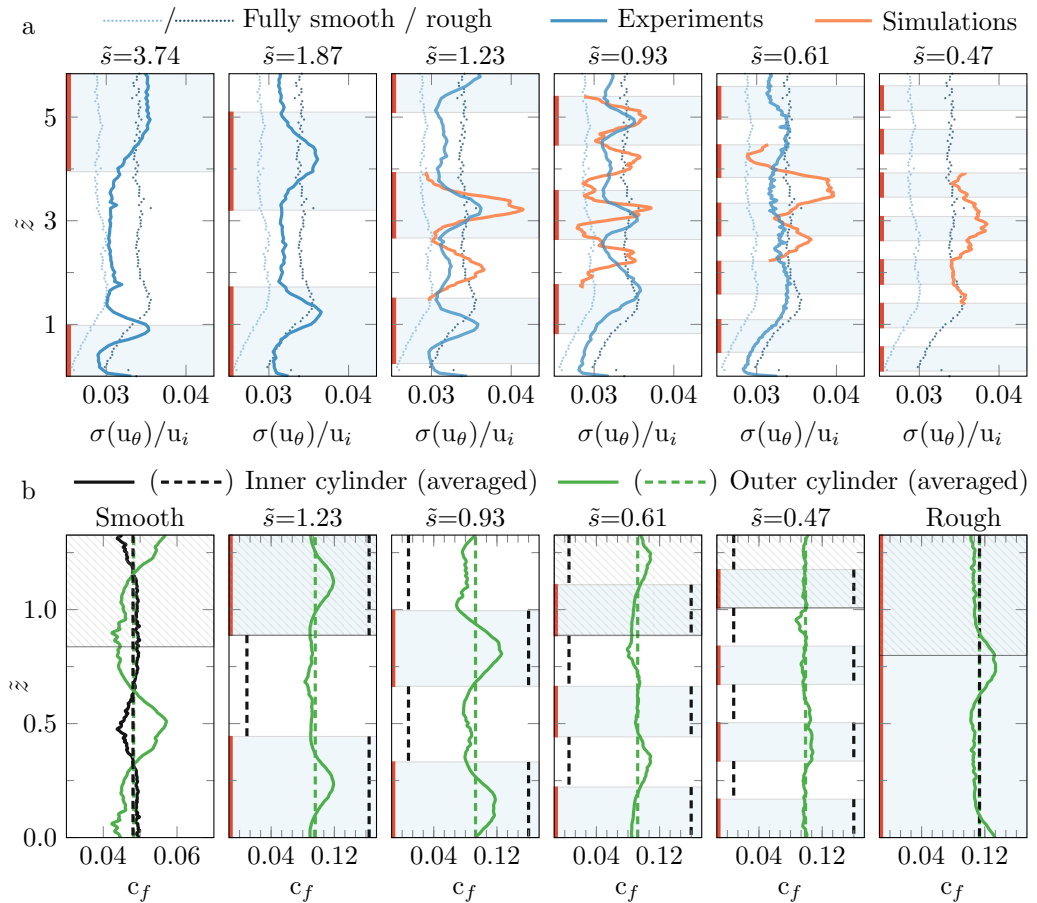


Figure 3: (a) Normalized standard deviation of the azimuthal velocity $\sigma(u_\theta)/u_i$ at midgap, as a function of $\tilde{z} = z/d$ for various \tilde{s} . $Ta = 1 \times 10^{12}$ for all experiments and $Ta = \mathcal{O}(10^9)$ for the DNSs. The enforced roughness pattern is indicated in red and a light blue shade. The signature of the roughness pattern is clearly visible in the bulk flow, both for the numerical simulations (orange) as for the experiments (blue). For $\tilde{s} = 0.61$, the roughness pattern does not leave a distinct imprint of its topology in the midgap flow statistics. (b) Local friction factor $c_f(\tilde{z})$ versus the axial height $\tilde{z} = z/d$ for $Ta = \mathcal{O}(10^9)$. The black lines show $c_f(\tilde{z})$ at the IC and the green line show $c_f(\tilde{z})$ at the OC. $c_{f,r}$ above the rough patches was calculated by subtracting the smooth average of $c_{f,s}$ from $C_f = \langle c_f(\tilde{z}) \rangle_L$ of the entire IC. Hatched regions indicate axially translated copies of the same data (including averages) – possible due to the periodic boundary condition in the axial direction – to allow for straightforward comparison. Imprints of the large secondary flows on the friction at the cylinder walls is observed, where impacting region experience a higher shear stress.

3. Results

3.1 Response of the Turbulent Taylor Vortices

In order to get a first insight on the effect of the roughness on the flow, we performed axial scans of the azimuthal flow velocity at midgap using LDA. Subsequently, we

calculated the standard deviation of the azimuthal velocity. In figure 3, we show the standard deviation of the azimuthal velocity $\sigma(u_\theta)$ normalized by the inner cylinder velocity u_i , as a function of the height, for various \tilde{s} . Here, the axial coordinate is normalized using the cylinder gap width d such that $\tilde{z} = z/d$. Figure 3 reveals that for the case of the largest stripe width ($\tilde{s} = 3.74$), the smooth section has, on average, a value of $\sigma(u_\theta)/u_i \approx 0.03$, slightly larger than we found for the fully smooth case (shown with the dotted light blue lines). Above the rough stripe, towards the center of the setup (i.e. for large \tilde{z}), $\sigma(u_\theta)$ gradually increases to a value of approximately $\sigma(u_\theta)/u_i \approx 0.04$. A similar, but not so clear trend can be seen at the lower roughness section ($\tilde{z} \approx 0.93$) of this case. However, this might be influenced by the lower bottom plate of the system.

When looking at the $\tilde{s} = 1.87$ case, we see very similar, however more pronounced dynamics. Azimuthal velocity fluctuations are promoted in regions where the roughness is present, as suggested by the appearance of local peaks centered at the position of the rough stripes. This effect is further seen for the cases of $\tilde{s} = 1.23$ and $\tilde{s} = 0.93$, where we observe similar profiles. At their smooth areas however, we also observe enhanced velocity fluctuations, albeit less pronounced than the locations above the rough patches. This effect is not seen for $\tilde{s} > 1.27$. For the final case with $\tilde{s} = 0.61$ these trends seem to fade away and we see that $\sigma(u_\theta)$ becomes more axially independent, i.e. the peaks are less pronounced, and do not seem to follow the topology of the roughness stripes.

The results of the DNSs, presented together with the experiments in figure 3 exhibit very similar behaviour. When normalized with u_i , we find that the standard deviation of the streamwise velocity show similar values as in the experiments. This is intriguing since the k/d values in the simulations are almost one order of magnitude larger than in the experiments. Above the rough stripes, we find enhanced $\sigma(u_\theta)/u_i$, whereas over smooth stripes we find diminished $\sigma(u_\theta)/u_i$. For $\tilde{s} = 0.61$ however, the trends are somewhat different. There, we find enhanced $\sigma(u_\theta)/u_i$ above the smooth region in the DNSs, which is explained by the recombination of plume ejection regions, forming one larger TTV above the smooth regions, see figure 5.

The findings presented in figure 3 show that the presence of the roughness affects the relative turbulence statistics in the bulk of the flow, far away from the roughness sublayer region (in contrast to homogeneous roughness in TC flow (Berghout *et al.* 2018)), reminiscent to what is found in studies of pipe and channel flow (Koeltzsch *et al.* 2002; Chung *et al.* 2018).

Figure 3(b) shows the axial variations of the friction factor $c_f(\tilde{z})$ (see section 1) on both the inner cylinder and the outer cylinder. The solid and dashed black lines represent $c_f(\tilde{z})$ measured on the inner cylinder, and the solid (green) lines represent $c_f(\tilde{z})$ on the outer cylinder. We average both in time and in the azimuthal direction. Significant variations in $c_f(\tilde{z})$ are observed which are linked to the orientation of the TTV. For impacting regions, *i.e.* plumes impacting on the inner cylinder boundary layer, the wall shear stress in the azimuthal direction is enhanced. When plumes eject from the inner cylinder boundary layer, also known as the ejecting regions, the shear stress is reduced. This, once more, illustrates the relative strength of the secondary flow (TTV) and the mean flow. For $\tilde{s} = 0.93$, the variations of the friction factor on the outer cylinder are even more pronounced, thus indicating that the strength of the TTV are enhanced with enforcing the spanwise variations in the roughness. For $\tilde{s} = 0.47$, the variations are not visible and the TTV are severely weakened, but still present, see figure 5.

To gain more insight into how the roughness alters the flow, we set out to measure the velocity field in the meridional plane using PIV at multiple heights. In figure 4, we show the temporal and azimuthally averaged radial velocity component u_r , normalized with u_i , in the spanwise wall-normal plane (\tilde{z} - \tilde{r}), where the radial coordinate is normalized such

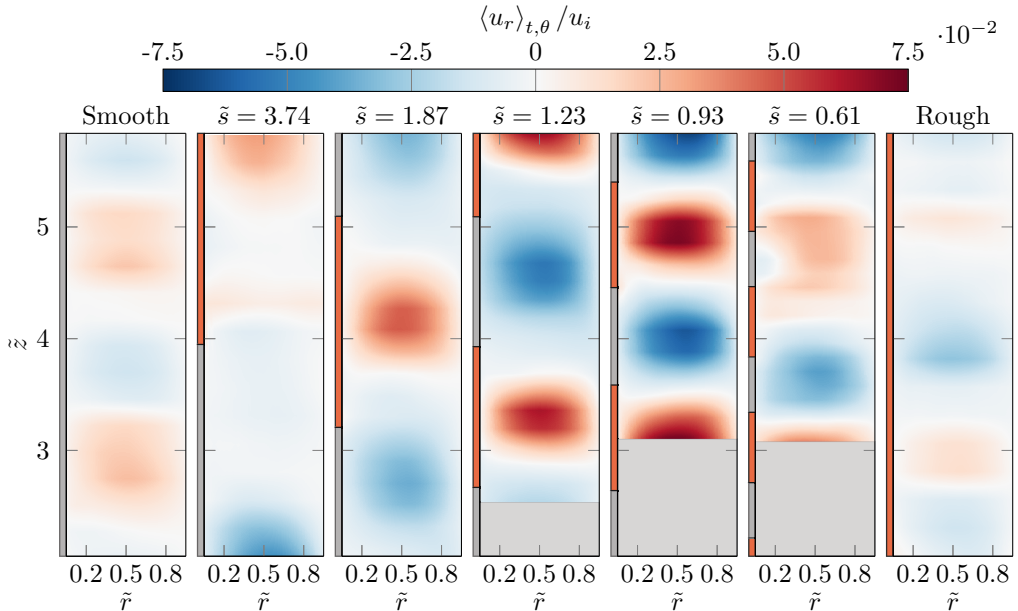


Figure 4: Temporal and azimuthal average of the radial velocity u_r , normalized with the inner cylinder azimuthal velocity u_i , obtained from experiments at $Ta = 1 \times 10^{12}$ using PIV for varying roughness stripe sizes \tilde{s} . A positive value of u_r denotes outflow, while a negative value denotes inflow, with respect to the inner cylinder. It can be seen that the rolls are pinned by the roughness and their wavelength changes with \tilde{s} . The red and gray areas at the left side of each plot indicate the positions of the rough and smooth areas, respectively. Note that the typical grain size is $k/d \approx 0.01$. The gray shaded areas in the gap represent unexplored heights.

that $\tilde{r} = (r - r_i)/d$. Figure 4 shows that for the case of $\tilde{s} = 3.74$, a very large structure can be seen, which consists of a large outflow region (positive u_r) around $\tilde{z} = 5.84$, while a large inflow region (negative u_r) is detected around $\tilde{z} = 2.10$. The situation is more pronounced for the cases of $\tilde{s} = 1.87$, $\tilde{s} = 1.23$, and $\tilde{s} = 0.93$, where a clear roll-like structure (i.e. the TTV) can be observed. Note that the radial component in the flow changes sign along the axial direction as it should in the presence of a TTV. What is rather remarkable is that the wavelength of the rolls λ changes for different values of \tilde{s} . For the large structure at $\tilde{s} = 3.74$, the normalized wavelength is $\tilde{\lambda} = \lambda/d \approx 4.01$. As \tilde{s} decreases to $\tilde{s} = 1.87$, $\tilde{\lambda} \approx 1.49$. At $\tilde{s} = 1.23$, the wavelength decreases to a value of $\tilde{\lambda} \approx 1.42$. At $\tilde{s} = 0.93$, $\tilde{\lambda} \approx 0.94$, and finally for the smallest value of $s = 0.61$, the wavelength increases slightly to $\tilde{\lambda} = 1.09$. We remind the reader the work of Huisman *et al.* (2014), who revealed that for counter-rotation ($-\omega_o/\omega_i \approx 0.4$), the average wavelength of the rolls could be either $\tilde{\lambda} = 1.46$ or $\tilde{\lambda} = 1.96$ depending on the *state* attained by the system. The current work shows that by an appropriate choice of \tilde{s} , the wavelength of the rolls can firstly, abandon its natural state; and secondly, it can be tuned within the range $\tilde{\lambda} \in [0.94, 4.01]$. The wavelengths described above were calculated by measuring the locations of two consecutive maxima and minima of $\langle u_r \rangle_{t,\theta,r_{bulk}}$ along z which are closest to midheight. Here, the symbol $\langle \cdot \rangle_{t,\theta,r_{bulk}}$ denotes average over time, the streamwise direction and the bulk region, i.e. $(r_{bulk} - r_i)/d \in [0.3, 0.7]$.

In addition, we observe that outflow regions (flow away from the IC) are created in axial regions where the roughness is located; and conversely, inflow regions (flow

towards the IC) are created in the smooth areas. Note that this orientation of the secondary flows is opposite to what is found in other canonical systems (e.g. pipe flow and channel flow (Willingham *et al.* 2014; Yang & Anderson 2017; Chung *et al.* 2018)), where one finds inflow regions above the rough stripes and outflow region above the smooth stripes. Consistent with findings in boundary layers however, is the correlation between low momentum pathways (LMPs) and outflow regions (Vanderwel & Ganapathisubramani 2015). Indeed we find that LMPs - with respect to the IC and located on top of the roughness - is associated with outflow regions, similar to Vanderwel & Ganapathisubramani although their Lego[®] roughness strips are much thinner and protrudes farther into the flow.

Another interesting observation is that since the driving is now from the BL rather than the bulk, the strength of the rolls changes depending on the value of \tilde{s} , as evidenced by the magnitude of $|u_r|$. In order to explore this feature in more detail, we quantify the strength of the rolls by $\tilde{u}_r' \equiv \sqrt{\langle (u_r/u_i)^2 \rangle_{t,\theta,r_{bulk},z_\lambda}}$ as a function of \tilde{s} . Here, the symbol $\langle \cdot \rangle_{t,\theta,r_{bulk},z_\lambda}$ denotes an average over time, the streamwise direction, the bulk region, and the axial region that defines the wavelength of a single roll z_λ . In figure 6(c), we show \tilde{u}_r' as a function of \tilde{s} , where we observe that the strength of the rolls increases with decreasing \tilde{s} for $\tilde{s} \in [0.93, 3.74]$. However at $\tilde{s} = 0.61$ the trend is broken, and we observe that \tilde{u}_r' decreases with respect to the case of $\tilde{s} = 0.93$.

In order to obtain more insight into the mechanism(s) that lead to the variation of $\tilde{\lambda}$ with \tilde{s} , we turn to DNS, albeit at a much lower Ta ($\approx 1.0 \times 10^9$), and much higher roughness height ($k/d \approx 0.1$). Since very large \tilde{s} cases are not feasible for DNS, we focus on matching the exact \tilde{s} in the lower range. We will show that, despite the $\mathcal{O}(10^3)$ difference in Ta, the same observations found in the numerics are also found in the experiments.

First, we look at the azimuthal velocity component. In figure 5, we plot the difference of the temporal and azimuthal average of the angular velocity $\langle \omega \rangle_{t,\theta}$ with respect to the temporal, azimuthal and, axial average of the angular velocity $\langle \omega \rangle_{t,\theta,z}$. This is done to emphasize the underlying organization of the TTVs. Here, we clearly observe that for all \tilde{s} , ejecting regions of angular velocity are originated in the rough stripes, similar to the preferential plume ejection sides at the tips of grooves in Zhu *et al.* (2016). These ejecting regions advect fluid from the roughness stripe on or at the inner cylinder towards the outer cylinder. These ejecting regions occur at each roughness stripe and as a consequence, an array of plume-like structures are formed along the axial direction. In TC flow (without roughness), plume-like structures are clear signatures of the presence of TTVs (Ostilla-Mónico *et al.* 2014c,b). A closer inspection of figure 5 reveals that for the largest value of $\tilde{s} = 1.23$, the plumes have enough separation not to interact among them. When \tilde{s} is decreased to $\tilde{s} = 0.93$, we observe that the plumes come closer, and can, in fact, interact with each other. At the lower $\tilde{s} = 0.61$ however, the situation is rather different. The rough patches are too close to each other to create individual ejecting regions and therefore, merge to a larger collective plume. For the $\tilde{s} = 0.61$ case, we observe in both, experiments and DNS that two ejecting regions, each located on top of a rough region, merge into a combined ejecting region. When \tilde{s} is decreased to a value of 0.47, even three ejecting regions are combined to a single large plume. These combined plumes drive TTV with a larger wave length, therefore, decreasing the effective momentum transfer. These observations help us to rationalize the change in the wavelength and strength of the rolls shown in figure 4. If \tilde{s} decreases, the plumes are effectively forced to come closer to each other; and as a result, the roll changes its wavelength and becomes stronger due to the added interaction of the plumes. In figure 5 we show $(\langle \omega \rangle_{t,\theta} - \langle \omega \rangle_{t,\theta,z})/\omega_i$, the same quantity discussed previously, albeit now for the experiments. Here, we can clearly see

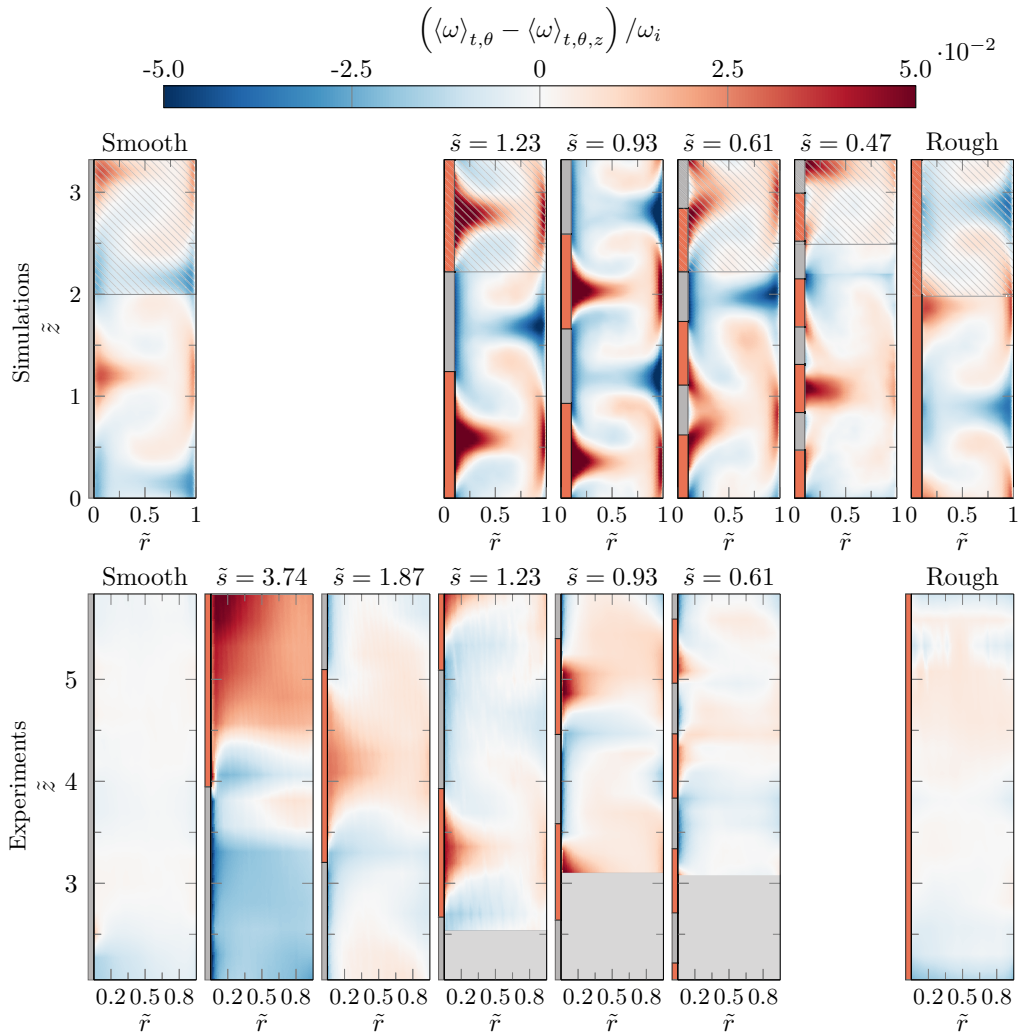


Figure 5: Deviation of the temporal and azimuthally averaged angular velocity $\langle \omega \rangle_{t,\theta}$ with respect to the temporal, azimuthal, and axial averaged angular velocity $\langle \omega \rangle_{t,\theta,z}$ obtained from DNS at $Ta \approx \mathcal{O}(10^9)$ (top), and experiments at $Ta = 1 \times 10^{12}$ (bottom), for various \tilde{s} explored. For experiments, \tilde{r} spans between $[0.05, 0.95]$. All fields are normalized with the angular velocity of the inner cylinder $\omega_i = u_i/r_i$. Positive values represent velocities that are closer to the IC velocity. The leftmost panel corresponds to the case of no roughness (smooth) while the rightmost panel is the case where the entire IC is uniformly rough. For better comparison, overlapping \tilde{s} cases for DNS and experiments are aligned vertically. Missing cases were not feasible in experiments or DNS. Hatched regions in the DNS figures indicate axially translated copies of the same data—possible due to the periodic boundary condition in the axial direction—to allow for straightforward comparison. The gray shaded areas in the gap represent unexplored heights. Ejecting regions can be seen in axial locations where the roughness is present. Notice the similarity of the flow structures between DNS and experiments.

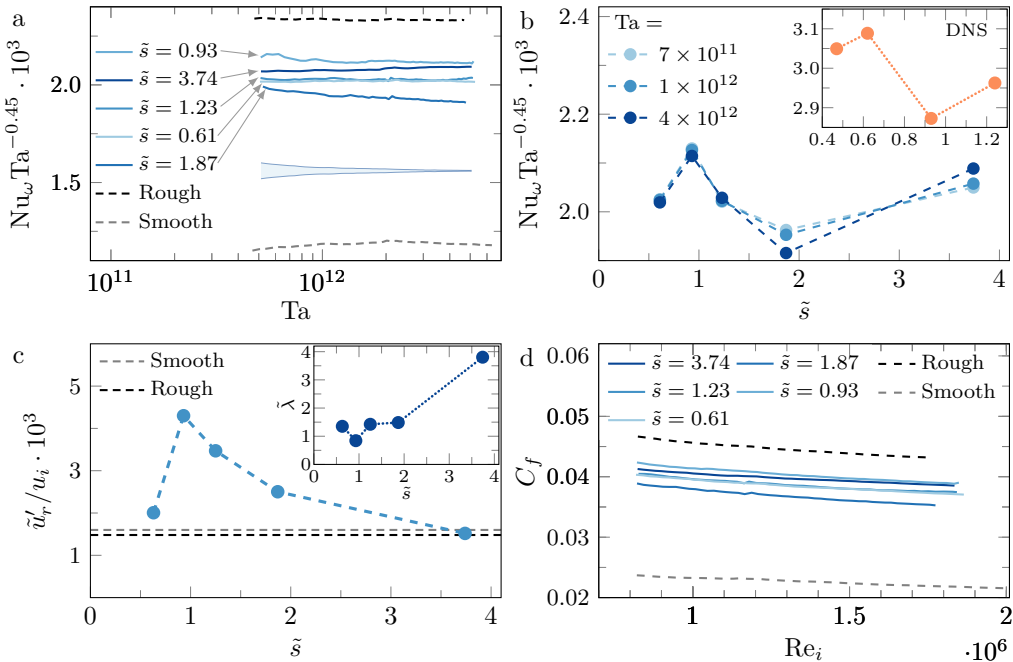


Figure 6: (a) Compensated Nusselt number $Nu_\omega Ta^{-0.45}$ as function of Ta for varying \tilde{s} . The shaded area indicates the error of the measurements, which can be seen to decrease with increasing driving strength. (b) Compensated Nusselt number $Nu_\omega Ta^{-0.45}$ as a function of \tilde{s} for three selected Ta . Here, an optimum value in the transport of angular momentum is observed close to $\tilde{s} \approx 1$. The inset in (b) shows the results obtained with the DNS ($Ta \approx 10^9$), where the maximum can be observed at a slightly lower \tilde{s} , namely $\tilde{s} \approx 0.6$. (c) The strength of the rolls, quantified as the normalized RMS of the radial velocity \tilde{u}'_r , as a function of \tilde{s} , obtained from the PIV experiments. The inset shows the wavelength of the TTV as function of \tilde{s} . (d) Friction coefficient C_f as a function of the driving strength, expressed with the Reynolds number Re_i , for various \tilde{s} .

that a similar mechanism takes place. Plume-like structures are originated at the centers of the roughness elements and interact with each other if the spacing (small \tilde{s}) is reduced.

The LDA, PIV and DNS explored in this section reveal that there is a mean effect of the spanwise-varying roughness on the large scale secondary flows that exist in turbulent TC flow. We have seen thus far that the roughness pins the rolls, and that their wavelength and strength can be tuned depending of the choice of \tilde{s} over a wide range of Ta , and a wide range of roughness heights h . However, how does the flow respond globally, i.e. the angular momentum transport, to this change in morphology? This will be addressed in the following section.

3.2 Global response

The global response of the TC system can be expressed with Nu_ω (equation 1.2) or with the related friction coefficient C_f . In figure 6(a), we show the compensated Nu_ω as a function of the driving strength Ta , where a scaling of $Nu_\omega \propto Ta^\alpha$, with $\alpha = 0.45$ is observed for all the \tilde{s} explored. The same data is represented as C_f versus Re_i in figure 6(d). In absence of roughness and within the same range of Ta , the scaling is found to be effectively $Nu_\omega \propto Ta^{0.39}$ (Paoletti & Lathrop 2011; van Gils *et al.* 2011; Huisman

et al. 2014). In contrast, when both of the solid walls are made uniformly rough (i.e. pressure drag dominates), the scaling asymptotes to the ultimate regime predicted by Kraichnan, *i.e.* $\text{Nu}_\omega \propto \text{Ta}^{0.5}$ (Kraichnan 1962; Zhu *et al.* 2018). In Zhu *et al.* (2018), the closest configuration to our study is the case of rough IC and smooth OC, for which an effective exponent $\alpha = 0.43$ was found. We note that this exponent is slightly smaller than the ones observed in the current study. The reason behind this is currently unknown. We notice, however, that the roughness type in our study is rather different. In this study we use spanwise-varying sand grain roughness, while the roughness in Zhu *et al.* (2018) is made of rib obstacles and is oriented perpendicular to the streamwise direction.

In order to connect the observed dynamics of the TTVs with the global response, we plot in figure 6(b) the compensated Nusselt number $\text{Nu}_\omega \text{Ta}^{-0.45}$ as a function of \tilde{s} for both the experiments and the numerics. We note that the exponent found for $\tilde{s} = 1.87$ ($\alpha = 0.44$) is nearly the same as $\alpha = 0.45$. We notice rather remarkably, the appearance of a maximum around $\tilde{s} \approx 0.93$ for the experiments, and $\tilde{s} = 0.61$ for the DNS (shown in the inset of figure 6(b)). We attribute the appearance of this peak to the strengthening of the TTVs, which is caused by the variation of \tilde{s} , and thus of $\tilde{\lambda}$. Explicitly, by lowering \tilde{s} , we can decrease the wavelength of the rolls, as seen in the inset of figure 6(c), thereby, bringing them closer together (see also section 3.1). As a consequence, in contrast the rolls are strengthened which leads to an enhancement of the angular momentum transport; and thus, the peak around $\tilde{s} = 0.93$. This peak is also visible in the normalized RMS of the radial velocity, \tilde{u}'_r , plotted in figure 6(c). With decreasing \tilde{s} , \tilde{u}'_r increases until an optimum is been reached around $\tilde{s} = 0.93$. Below the optimum, \tilde{u}'_r drops drastically to much lower values. This optimum is also observed by Huisman *et al.* (2014), though the mechanism leading to optimum transport there is quite different. While the rolls in their study are enhanced by counter-rotating the OC; in our case, the rolls are strengthened by forcing $\tilde{\lambda}$ below their natural wavelength due to the right choice of the size of the spanwise varying roughness \tilde{s} . This is also supported by the observation that the magnitude of the radial velocity shows a maximum around $\tilde{s} = 0.93$, as shown in figure 6(c). We note, however, that the torque is not measured throughout the entire axial length of the cylinders $L = 927$ mm, but in a smaller section of length $L_{\text{mid}} = 536$ mm. As a result, the large structure identified previously for the case of $\tilde{s} = 3.74$ ($\tilde{\lambda} = 4.01$), does not fit entirely in the measurement section (see the first panel of figure 4). As a result, the Nusselt number corresponding to this case could be under or overestimated.

We also note that in the case of the numerics, the position of the maximum is different than in the experiments. We attribute this to a combination of two effects. On the one hand the DNS is performed at a lower Ta, which has an effect on the natural wavelength of the rolls as it was shown by Chouippe *et al.* (2014), who show that for similar values of η , the wavelength of the rolls can decrease with decreasing Ta. On the other hand, the axial domain of the DNS is bounded by $\Gamma \in [2.08, 3.32]$, which gives rise to limited box-sizes. Thus, when \tilde{s} is varied, the rolls could suffer from an additional *constraint* due to the limited axial domain. In addition to this discrepancy, we also note that the scaling in the range of Ta at which the DNS is done ($\approx 1.0 \times 10^9$), is not known a priori. In absence of a better choice, we compensate the numerical data using the same exponent as in the experiments (figure 6(b)). However, we note that this exponent might be different due to the 2 decades of separation in Ta between the numerics and experiments, as was also shown by Zhu *et al.* (2018). We would like to emphasize, however, that in spite of these discrepancies, a maximum in angular momentum transport is observed for a given \tilde{s} in both the experiments and the numerics, which is solely a consequence of the varying axial wavelength of the TTV, dictated by the spanwise-varying roughness.

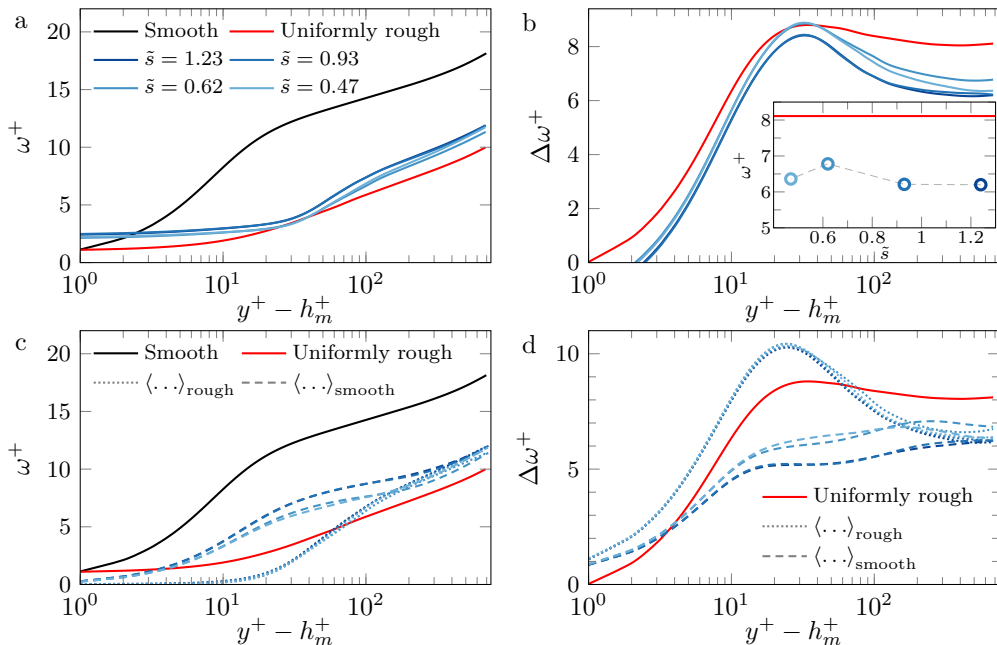


Figure 7: (a) Angular velocity ω^+ profiles in the reference frame of the IC versus the wall normal distance $y^+ - h_m^+$ for various \tilde{s} , where h_m^+ is the virtual origin and equals the melt-down (i.e. mean) height $h_m/d \approx 0.2$ of the rough surface and $y^+ = (r - r_i)/\delta_\nu$. The solid black line represents the uniformly rough case. (b) Angular velocity shift $\Delta\omega^+$ as a function of $y^+ - h_m^+$ for varying \tilde{s} . In the inset of (b), we show the angular velocity shift $\Delta\omega^+$ versus the wall normal distance $y^+ - h_m^+$. Here, we observe a maximum downwards shift of the angular velocity profile for the simulation where we cover the entire inner cylinder with sandpaper roughness (i.e. uniformly rough). (c) The angular velocity conditioned on the axial location: above smooth surface ($\langle \omega^+ \rangle_{\text{smooth}}$) and rough surface ($\langle \omega^+ \rangle_{\text{rough}}$). (d) The angular velocity shifts conditioned on the axial location: above smooth surface ($\langle \Delta\omega^+ \rangle_{\text{smooth}}$) and rough surface ($\langle \Delta\omega^+ \rangle_{\text{rough}}$). We conclude that the plumes originating from the roughness elements lead to enhanced mixing of streamwise momentum, and hence a downwards shift of the velocity profiles. Further away from the wall, the bulk is well-mixed and the streamwise profiles above smooth and rough wall locations converge to a similar value.

3.3 Velocity profiles

Having discussed the dynamics of the TTVs and the corresponding global response, in terms of the dimensionless torque, we now set out to study the streamwise, angular, velocity profiles (rather than the azimuthal profiles, as discussed in Grossmann *et al.* (2014) and Berghout *et al.* (2018)). To allow for straightforward comparison between the respective velocity profiles, we run the DNS at constant friction Reynolds number $Re_\tau = 690 \pm 10$. The profiles are then temporally, azimuthally, and axially averaged $\omega^+ = \langle \omega \rangle_{t,\theta,z} / \omega_\tau$. The profiles still exhibit a logarithmic region when averaged over the entire axial coordinate. Figure 5 shows however that the TTVs in the flow, following the spanwise-varying roughness, do not exhibit any outer similarity. Deviations of the azimuthal and temporal averages from the mean logarithmic profiles are found up to $\Delta\omega^+ \approx 2$.

For turbulent flows over rough walls, the streamwise velocity profiles retain their logarithmic form. However, the hallmark effect of rough walls is a downwards shift of this region (for any drag increasing surface), which can also be understood as an increase of the skin friction factor C_f (Hama 1954). Figure 7(a) shows the angular velocity profiles ω^+ as a function of $(y^+ - h_m^+)$, where h_m^+ is the virtual origin and equals the melt-down (i.e. mean) height of the rough surface and $y^+ = (r - r_i)/\delta_\nu$. We choose the melt-down height of the roughness over the full inner cylinder as the virtual origin. In figure 7(b) we show the velocity shift versus the wall normal distance. The inset gives a vertical cut at $y^+ = Re_\tau$. It is evident that also in this representation, an optimum in the velocity shift, and thus in C_f can be observed. The position of this maximum ($\tilde{s} = 0.61$) is the same as the one obtained from the angular momentum transport (see section 3.2).

In figures Figure 7c and Figure 7d we employ conditional averaging of the angular velocity profiles over the smooth $\langle \dots \rangle_{\text{smooth}}$ and rough $\langle \dots \rangle_{\text{rough}}$ axial locations. The wall shear stress in the viscous normalization is taken over the entire axial height L of the inner cylinder. h_m^+ is also taken as a local variable. We already deduce from figure 5 that significant variations in the temporal and azimuthal average of the velocity profiles are expected, at least close to the roughness. Indeed we find that for all \tilde{s} the region above the roughness is better mixed, due to the presence of plume-like structures originating from the rough surface. The angular velocity profiles is thus shifted downwards in comparison to the average over the entire IC. For the smooth wall conditioned profiles, we observe the opposite, such that the profiles lay higher.

The merging of plumes from different rough patches into a large scale coherent TTV is also observed in the cross-over of $\langle \omega^+ \rangle_{\text{smooth}}$ and $\langle \omega^+ \rangle_{\text{rough}}$ for $\tilde{s} = 0.61$ in Figure 7d at $y^+ - h_m^+ \approx 210$. Further into the bulk flow, turbulent processes mix out the inhomogeneous effects of rough wall attached plumes, and the angular velocity profiles converge to similar values. However, we note that even at $y^+ - h_m^+ = Re_\tau$, $\langle \omega^+ \rangle_{\text{smooth}}$ and $\langle \omega^+ \rangle_{\text{rough}}$ differ to ≈ 0.5 .

4. Conclusions and outlook

In conclusion, we have investigated, both numerically and experimentally, large Taylor number Taylor-Couette flow in the presence of spanwise-varying roughness, which consists of an arrangement of stripes of width \tilde{s} , that covers the entire circumference of the inner cylinder. In the experiments, the stripes were made from sandpaper, while in the numerics a confocal microscopy scan of the surface was implemented by means of the immersed boundary method (IBM).

Remarkably, we have found that by varying \tilde{s} in the range $\tilde{s} = [0.47, 3.74]$ we can alter the axial wavelength of the turbulent Taylor vortices within the range $\tilde{\lambda} \in [0.94, 4.01]$, even if the roughness height was very low ($k/d \approx 0.01$). This manipulation was observed to hold in a range of three decades in Ta ($\mathcal{O}(10^9) - \mathcal{O}(10^{12})$).

In the experiments, the scaling of the Nusselt number with the driving strength was found to be effectively $Nu_\omega \propto Ta^{0.45}$ for $Ta \in [5 \times 10^{11}, 5 \times 10^{12}]$. The experiments and DNSs also revealed that inflow regions ($u_r < 0$) originated between the rough stripes, where the inner cylinder was hydrodynamically smooth (in contrast to secondary flows induced by spanwise-varying roughness in channel flow, where the orientation of the vortices is reversed (Chung *et al.* 2018)). Conversely, at the center of the rough stripes, we observed the creation of outflow regions ($u_r > 0$) which were accompanied by the promotion of azimuthal velocity fluctuations $\sigma(u_\theta)$ at midgap. At these axial locations (center of rough stripes), we observed, in both the numerics and experiments, the emission of plume-like structures, which are responsible for the creation and pinning

of the rolls. Since the coverage of the roughness was fixed, we showed that by reducing \tilde{s} , we can effectively bring these structures closer, and enhance the interaction of the rolls, as evidenced by the increment in $|u_r|$. As a consequence of this interaction, the flow responded globally by inducing a maximum of angular momentum transport at $\tilde{s} = 0.93$ in the experiments, and $\tilde{s} = 0.61$ in the numerics.

We wish to stress that in this study the change in the morphology of the large-scale structures is only due to the spanwise-varying roughness (of very low height) and not by a change of Γ or η , which opens the possibility of exploring different configurations in which the rolls can be tuned at such large turbulence levels.

Many questions arise from the aforementioned observations. Understanding the mechanisms leading to the merging of plume ejection regions, and accompanied parameter boundaries at which this occurs, would lead to a further insight into the dynamics of the TTVs. Furthermore, it would be intriguing, in the spirit of Bakhuis *et al.* (2018), to study the influence of spanwise-varying regions of idealized high and low wall shear stress, without geometrical induced disturbances. It is an open question whether one could also alter λ , without the interaction of the plumes.

Acknowledgements

We would like to thank Jelle Will and Dominik Krug for various stimulating discussions. We like to thank José Encarnación Escobar for performing the confocal microscopy measurements and Gert-Wim Bruggert for technical support. This work was funded by Natural Science Foundation of China under grant no. 91852202, VIDI grant No. 13477, STW, FOM, MCEC, and the Netherlands Organisation for Scientific Research (NWO). This project is also partially funded by the Priority Programme SPP 1881 Turbulent Superstructures of the Deutsche Forschungsgemeinschaft. We also acknowledge PRACE for awarding us access to MareNostrum based in Spain at the Barcelona Supercomputing Center (BSC) under PRACE project number 2017174146. This work was partly carried out on the national e-infrastructure of SURFsara, a subsidiary of SURF cooperation, the collaborative ICT organization for Dutch education and research.

REFERENCES

- ANDERSON, W., BARROS, J. M., CHRISTENSEN, K. T. & AWASTHI, A. 2015 Numerical and experimental study of mechanisms responsible for turbulent secondary flows in boundary layer flows over spanwise heterogeneous roughness. *J. Fluid Mech.* **768**, 316–347.
- BAKHUIS, D., OSTILLA MÓNICO, R., VAN DER POEL, E. P., VERZICCO, R. & LOHSE, D. 2018 Mixed insulating and conducting thermal boundary conditions in Rayleigh-Bénard convection. *J. Fluid Mech.* **835**, 491–511.
- BARROS, J. M. & CHRISTENSEN, K. T. 2014 Observations of turbulent secondary flows in a rough-wall boundary layer. *J. Fluid Mech.* **748**, R1.
- VAN DEN BERG, T. H., DOERING, C. R., LOHSE, D. & LATHROP, D. P. 2003 Smooth and rough boundaries in turbulent Taylor-Couette flow. *Phys. Rev. E* **68**, 036307.
- BERGHOUT, P., ZHU, X., CHUNG, D., VERZICCO, R., STEVENS, R. J. A. M. & LOHSE, D. 2018 Direct numerical simulations of Taylor-Couette turbulence: the effect of sand grain roughness. <https://arxiv.org/pdf/1812.02265.pdf> .
- BRADSHAW, P. 1987 Turbulent secondary flows. *Annu. Rev. Fluid Mech.* **19**, 53–74.
- CADOT, O., COUDER, Y., DAERR, A., DOUADY, S. & TSINOBER, A. 1997 Energy injection in closed turbulent flows: Stirring through boundary layers versus inertial stirring. *Phys. Rev. E* **56**, 427–433.
- CHOUPIPE, A., CLIMENT, E., LEGENDRE, D. & GABILLET, C. 2014 Numerical simulation of bubble dispersion in turbulent Taylor-Couette flow. *Phys. Fluids* **26**, 043304.

- CHUNG, D., MONTY, J. P. & HUTCHINS, N. 2018 Similarity and structure of wall turbulence with lateral wall shear stress variations. *J. Fluid Mech.* **847**, 591–613.
- ECKHARDT, B., GROSSMANN, S. & LOHSE, D. 2007 Torque scaling in turbulent Taylor–Couette flow between independently rotating cylinders. *J. Fluid Mech.* **581**, 221–250.
- FADLUN, E., VERZICCO, R., ORLANDI, P. & MOHD-YUSOF, J. 2000 Combined Immersed-Boundary Finite-Difference Methods for Three-Dimensional Complex Flow Simulations. *J. Comput. Phys.* **161**, 35–60.
- FLACK, K. A. & SCHULTZ, M. P. 2010 Review of hydraulic roughness scales in the fully rough regime. *J. Fluids Eng.* **132**, 041203.
- GROSSMANN, S., LOHSE, D. & SUN, C. 2014 Velocity profiles in strongly turbulent Taylor–Couette flow. *Phys. Fluids* **26**, 025114.
- GROSSMANN, S., LOHSE, D. & SUN, C. 2016 High–Reynolds Number Taylor–Couette Turbulence. *Annu. Rev. Fluid Mech.* **48**, 53–80.
- HAMA, F. 1954 Boundary-layer characteristics for smooth and rough surfaces. *Trans. Soc. Nav. Archit. Mar. Engrs* **62**, 333–358.
- HINZE, J. O. 1967 Secondary currents in wall turbulence. *Phys. Fluids* **10**, S122.
- HINZE, J. O. 1973 Experimental investigation on secondary currents in the turbulent flow through a straight conduit. *Appl. Sci. Res.* **28**, 453–465.
- HUISMAN, S. G., VAN GILS, D. P. & SUN, C. 2012 Applying laser Doppler anemometry inside a Taylor–Couette geometry using a ray-tracer to correct for curvature effects. *Eur. J. Mech. B-Fluids* **36**, 115–119.
- HUISMAN, S. G., VAN DER VEEN, R. C., SUN, C. & LOHSE, D. 2014 Multiple states in highly turbulent Taylor–Couette flow. *Nat. Comm.* **5**, 3820.
- IACCARINO, G. & VERZICCO, R. 2003 Immersed boundary technique for turbulent flow simulations. *Appl. Mech. Rev.* **56**, 331–347.
- JIMÉNEZ, J. 2004 Turbulent flows over rough walls. *Annu. Rev. Fluid Mech.* **36**, 173–196.
- KOELTZSCH, K., DINKELACKER, A. & GRUNDMANN, R. 2002 Flow over convergent and divergent wall riblets. *Exp. Fluids* **33**, 346–350.
- KRAICHNAN, R. H. 1962 Turbulent thermal convection at arbitrary Prandtl number. *Phys. Fluids* **5**, 1374.
- MEDJNOUN, T., VANDERWEL, C. & GANAPATHISUBRAMANI, B. 2018 Characteristics of turbulent boundary layers over smooth surfaces with spanwise heterogeneities. *J. Fluid Mech.* **838**, 516–543.
- MEJIA-ALVAREZ, R. & CHRISTENSEN, K. T. 2013 Wall-parallel stereo particle-image velocimetry measurements in the roughness sublayer of turbulent flow overlying highly irregular roughness. *Phys. Fluids* **25**, 115109.
- NIKURADSE, J. 1933 Laws of flow in rough pipes. *NACA Tech. Mem.* **1292**.
- NUGROHO, B., HUTCHINS, N. & MONTY, J. 2013 Large-scale spanwise periodicity in a turbulent boundary layer induced by highly ordered and directional surface roughness. *Int. J. Heat Fluid Fl.* **41**, 90–102.
- OSTILLA-MÓNICO, R., HUISMAN, S. G., JANNINK, T. J. G., VAN GILS, D. P. M., VERZICCO, R., GROSSMANN, S., SUN, C. & LOHSE, D. 2014a Optimal Taylor–Couette flow: radius ratio dependence. *J. Fluid Mech.* **747**, 1–29.
- OSTILLA-MÓNICO, R., VAN DER POEL, E. P., VERZICCO, R., GROSSMANN, S. & LOHSE, D. 2014b Exploring the phase diagram of fully turbulent Taylor–Couette flow. *J. Fluid Mech.* **761**, 1–26.
- OSTILLA-MÓNICO, R., VAN DER POEL, R. P., VERZICCO, R., GROSSMANN, S. & LOHSE, D. 2014c Boundary layer dynamics at the transition between the classical and the ultimate regime of Taylor–Couette flow. *Phys. Fluids* **26**, 015114.
- PAOLETTI, M. S. & LATHROP, D. P. 2011 Angular momentum transport in turbulent flow between independently rotating cylinders. *Phys. Rev. Lett.* **106**, 024501.
- VAN DER POEL, E. P., OSTILLA-MÓNICO, R., DONNERS, J. & VERZICCO, R. 2015 A pencil distributed finite difference code for strongly turbulent wall-bounded flows. *Comp. Fluids* **116**, 10–16.
- REN, H. & WU, Y. 2011 Turbulent boundary layers over smooth and rough forward-facing steps. *Phys. Fluids* **23**, 045102.

- SCHULTZ, M. P. 2007 Effects of coating roughness and biofouling on ship resistance and powering. *Biofouling* **23**, 331–341.
- STRINGANO, G., PASCAZIO, G. & VERZICCO, R. 2006 Turbulent thermal convection over grooved plates. *J. Fluid Mech.* **557**, 307–336.
- TAYLOR, G. I. 1923 Stability of a viscous liquid contained between two rotating cylinders. *Proc. Royal Soc. Lond. A* **102**, 541–542.
- TOWNSEND, A. A. R. 1976 *The structure of turbulent shear flow*. Cambridge University Press.
- VAN GILS, D. P., BRUGGERT, G.-W., LATHROP, D. P., SUN, C. & LOHSE, D. 2011 The Twente turbulent Taylor-Couette (T³C) facility: strongly turbulent (multiphase) flow between independently rotating cylinders. *Rev. Sci. Instr.* **82**, 025105.
- VAN GILS, D. P. M., HUISMAN, S. G., GROSSMANN, S., SUN, C. & LOHSE, D. 2012 Optimal Taylor–Couette turbulence. *J. Fluid Mech.* **706**, 118–149.
- VANDERWEL, C. & GANAPATHISUBRAMANI, B. 2015 Effects of spanwise spacing on large-scale secondary flows in rough-wall turbulent boundary layers. *J. Fluid Mech.* **774**, R2.
- VAN DER VEEN, R. C. A., HUISMAN, S. G., DUNG, O.-Y., TANG, H. L., SUN, C. & LOHSE, D. 2016 Exploring the phase space of multiple states in highly turbulent Taylor-Couette flow. *Phys. Rev. Fluids* **1**, 024401.
- VERZICCO, R. & ORLANDI, P. 1996 A finite-difference scheme for three-dimensional incompressible flow in cylindrical coordinates. *J. Comput. Phys.* **123**, 402–413.
- WANG, Z.-Q. & CHENG, N.-S. 2006 Time-mean structure of secondary flows in open channel with longitudinal bedforms. *Adv. Water Resour.* **29**, 1634–1649.
- WILLINGHAM, D., ANDERSON, W., CHRISTENSEN, K. T. & BARROS, J. M. 2014 Turbulent boundary layer flow over transverse aerodynamic roughness transitions: Induced mixing and flow characterization. *Phys. Fluids* **26**, 025111.
- YANG, J. & ANDERSON, W. 2017 Numerical study of turbulent channel flow over surfaces with variable spanwise heterogeneities: Topographically-driven secondary flows affect outer-layer similarity of turbulent length scales. *Flow Turbul. Combust.* **100**, 1–17.
- ZHU, X., OSTILLA-MÓNICO, R., VERZICCO, R. & LOHSE, D. 2016 Direct numerical simulation of Taylor–Couette flow with grooved walls: torque scaling and flow structure. *J. Fluid Mech.* **794**, 746–774.
- ZHU, X., VERSCHOOF, R. A., BAKHUIS, D., HUISMAN, S. G., VERZICCO, R., SUN, C. & LOHSE, D. 2018 Wall roughness induces asymptotic ultimate turbulence. *Nat. Phys.* **14**, 417–423.
- ZHU, X., VERZICCO, R. & LOHSE, D. 2017 Disentangling the origins of torque enhancement through wall roughness in Taylor–Couette turbulence. *J. Fluid Mech.* **812**, 279–293.